

Heterogeneity and patterning in the quasi-static behavior of granular materials

Matthew R. Kuhn

Abstract Heterogeneity is classified in five categories—topologic, geometric, kinematic, static, and constitutive—and the first four categories are investigated in a numerical DEM simulation of biaxial compression. The simulation experiments show that the topology and geometric fabric become more variable during loading. The measured fluctuations in inter-particle movements are large, they increase with loading, and they extend to distances of at least eight particle diameters. Deformation and rotation heterogeneity are large and are expressed in spatial patterning. Stress heterogeneity is moderate throughout loading.

Keywords: Granular material, Heterogeneous material, Patterning, Microstructure, Discrete Element Method

1 Introduction

Perhaps the most distinguishing characteristic of granular materials is their internal heterogeneity, particularly when viewed at the micro-scale of individual particles or particle clusters. Granular materials often consist of a wide range of particle sizes and shapes, and these particles are usually arranged in an irregular manner. This geometric and topologic multiformity produce nonuniform distributions of internal force and deformation, which are often expressed in spatial and temporal patterning. In the paper, we catalog the many forms in which heterogeneity may be manifest, and we provide a classification scheme for its measurement. Examples of several forms of heterogeneity are presented, and certain expressions of their evolution and spatial patterning are described. Although the proposed classification scheme applies to both two- and three-dimensional (2D and 3D) granular materials, to particles of arbitrary shape and composition, to both sparse and dense packings, and to both dynamic and quasi-static deformations, the paper illustrates the classification within

Received: date / Revised version: date

Matthew R. Kuhn

Dept. of Civil and Env. Engineering
School of Engineering
University of Portland
5000 N. Willamette Blvd., Portland, OR 97203, U.S.A.,
kuhn@up.edu, fax 503-943-7316, tel 503-943-7361

Send offprint requests to: Matthew R. Kuhn

a two-dimensional framework and with a 2D example of the quasi-static deformation of a dense disk assembly.

In Section 2 we consider a classification scheme for heterogeneity and the various forms in which it can be expressed and measured. Section 3 describes the simulation methods that are used to explore several forms of heterogeneity. In the same section, we also consider a means of measuring the heterogeneity of vector and tensor objects. Section 4 presents experimental results and characterizes several types of heterogeneity and their evolution during biaxial compression.

2 Classifying heterogeneity

Table 1 gives a classification of material characteristics that can manifest heterogeneity in granular materials. The table references sample experimental studies in which these characteristics have been measured, although the short lists of references are far from exhaustive. The characteristics in the table are organized within a hierarchy of heterogeneity categories: topologic, geometric, kinematic, static, and constitutive. These categories are described in a general manner in the next paragraph. Table 2 presents a short list of informational forms that can be used for describing each characteristic. The arrangement of the forms in Table 2 reflects their complexity and the usual historical order in which measurements have been proposed and collected. The simplest form of information is some measure of central tendency: a mean, median, or modal value. Heterogeneity implies diversity and fluctuation, and this dispersion in measured values can be expressed as a variance or standard deviation, with standard graphical means such as histograms, or by fitting experimental results to an appropriate probability distribution. Of greater complexity are measurements of temporal correlation (e.g. rates of change) and spatial correlation. The most complex data analyses can also disclose the spatial and temporal patterning of heterogeneity. The paper presents data on the six characteristics that are accompanied by section numbers in Table 1, and these characteristics are explored with a range of the informational forms that are given in Table 2.

Table 1 begins with topologic characteristics, which concern the arrangement of the particles and their contacts, but without reference to their position, size, or orientation. This information can be expressed as a *particle graph* for both 2D and 3D assemblies, which gives the topologic connectivity of the particles in a packing, as ex-

Table 1. Heterogeneity categories and references to experimental studies

| Category ^a | References |
|-----------------------------|--|
| Topologic (4.1) | |
| Coordination number | [1, 2, 3, 4] ^b , [5, 6, 7, 8, 9, 10, 11] ^e |
| Valence | [12, 9] ^b |
| Geometric | |
| Grain size | |
| Grain shape | |
| Grain orientation | [13, 14, 15], [16, 17] ^b |
| Void ratio | [18], [3, 19, 20] ^b , [20] ^c , [21, 22, 23, 24, 25] ^d |
| Void size/shape | [26] ^b |
| Branch vector orientation | [13, 15, 27, 28], [29] ^b , [6, 14, 30, 31] ^e |
| Branch vector length | [4], [32] ^c |
| Fabric tensor (4.2) | [33, 34], [8, 7, 11] ^e |
| Loop tensor | [9, 35], [26] ^b |
| Kinematic | |
| Particle movement | [36], [37] ^b , [38, 39] ^c , [9, 40, 41] ^d |
| Inter-particle motion (4.3) | [42, 32], [9, 43] ^d |
| Particle rotation (4.5) | [6, 30, 31, 37, 41] ^b , [9, 18, 23, 36] ^d |
| Deformation (4.4) | [37] ^b , [21, 30, 9, 44] ^d |
| Static | |
| Contact force | [36, 45, 46, 47], [4, 48, 49, 50, 51, 52, 53, 54, 55] ^b , [53, 55] ^b , [56, 46, 23, 36] ^d , [10] ^e |
| Force potential | [39] ^c |
| Stress (4.6) | [57, 58] ^b |
| Constitutive | [59, 60] ^b |

^a Section numbers (*.*) refer to the experimental results in this paper

^b Includes statistical measures, e.g. including standard deviations or histograms

^c Includes spatial correlations

^d Includes spatial patternings

^e Includes rates of changes or temporal patterning

Table 2. Analyses of heterogeneity

| Informational forms | Examples |
|---------------------------------|--|
| Central tendency | Mean, median, modes |
| Dispersion | Standard deviation, variance, coefficient of variation, histograms, probability and cumulative distributions, quartile plots |
| Spatial correlation | n-point correlations, correlation lengths |
| Temporal correlation | Rates of change |
| Spatial and temporal patterning | Spatial plots, time series analyses, spatial domain transforms |

plained in [61]. The paper presents data on the variation in local topology and its evolution during loading. A discrete metric is also proposed as a means of tracking inter-particle processes between distant particles. Geometric information includes the additional descriptors of length, shape, and angle, which relate to the positional arrangements, orientations, and sizes of particles. Together, topology and geometry describe the *fabric* of a granular assembly. The paper characterizes the evolution of one form of heterogeneity in this fabric. Kinematic information (Table 1) concerns the movements and rotations of particles, relative inter-particle movements, and the local deformations within small groups of particles. The paper gives examples of heterogeneous movements and deformations, the spatial correlation of inter-particle movements, and the patterning of local rotations and deformations. Static (or statical) information (Table 1) involves the transmission of force and stress within a material, and the paper depicts the local diversity of stress and its evolution during loading. Table 1 also includes the category of *constitutive* heterogeneity (or, perhaps, mechanical heterogeneity), which would involve the diversity in local material stiffness. Except for simple two-particle models that rely on uniform strain assumptions, there is, as of yet, no consistent vocabulary or experimental methods for measuring and characterizing this form of heterogeneity. The reader is referred to the recent work of Gaspar and Koenders [59] and Gaspar [60], which may provide a needed framework for characterizing constitutive heterogeneity.

As a simple example of the classification scheme in Table 2, we could consider the diversity of grain size in a granular material. Methods for measuring and describing particle size, such as sieving methods, are standardized and widely applied, so that references to these methods are excluded from Table 2. These methods can readily depict a representative (central) grain size as well as the dispersion of sizes. Certain processes, such as shearing and compression, can cause particle breakage, which could be measured with temporal correlations of the size distribution. Processes that promote size segregation could be studied with methods that reveal the spatial correlation of size. Size segregation usually leads to a spatial patterning of the local size distribution, and processes that produce a periodic recurrence in such patterning would lead to both spatial and temporal patterning.

3 Methods and notation

A conventional implementation of the Discrete Element Method (DEM) was used to simulate the quasi-static behavior of a large 2D granular assembly and to illustrate different manifestations of internal heterogeneity and their evolution.

3.1 Simulation methods

The study employs a square assembly containing 10,816 circular disks of multiple diameters. The disk sizes are randomly distributed over a fairly small range of between

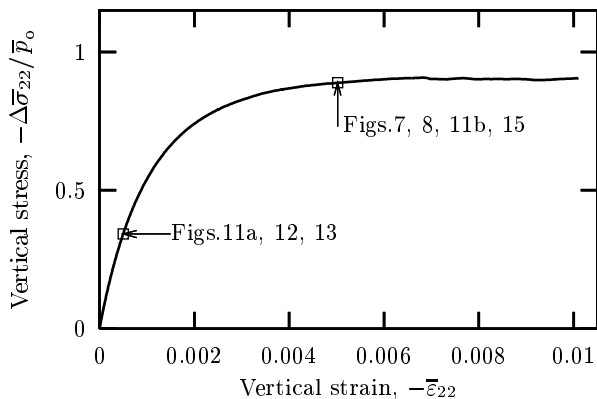


Fig. 1. Evolution of the average compressive stress within the assembly of 10,816 circular disks during biaxial compression.

$0.56\bar{D}$ and $1.7\bar{D}$, where \bar{D} is the mean particle diameter. The material was created by slowly and isotropically compacting a sparse arrangement of particles, during which friction between particle pairs was disallowed (friction was later restored for biaxial compression tests). This compaction technique produced a material that was dense, random, and isotropic, at least when viewed at a macro-scale. The average initial void ratio was 0.1715 (solid fraction of 0.854), the average coordination number was 3.95, and the average overlap between neighboring particles was about 9×10^{-4} of \bar{D} . The assembly was surrounded by periodic boundaries, a choice that would eliminate the topologic and geometric nonuniformity that might otherwise occur in the vicinity of rigid platens or assembly corners. The initial height and width of the assembly were each about $102\bar{D}$.

All examples of heterogeneity were collected from a single loading test of biaxial compression. The height of the assembly was reduced at a constant rate of compressive strain ($\dot{\epsilon}_{22} < 0$), while maintaining a constant average horizontal stress ($\dot{\sigma}_{11} = 0$). About 200,000 time steps were required to reach the final vertical strain, $\bar{\epsilon}_{22}$, of -0.01 , and at this rate of loading, the average imbalance of force on a particle was less than 1×10^{-4} times the average contact force.

During biaxial compression, a simple force mechanism was employed between contacting particles. Linear normal and tangential contact springs were assigned equal stiffnesses ($k_n = k_t$), and slipping between particles would occur whenever the contact friction coefficient of 0.50 was attained.

The average, macro-scale mechanical behavior is shown in Fig. 1, which gives the dimensionless compressive stress $\Delta\bar{\sigma}_{22}/\bar{p}_o$, where \bar{p}_o is the initial mean stress, $\bar{p}_o = (\bar{\sigma}_{11} + \bar{\sigma}_{22})/2$. This initial mean stress was about 5×10^{-4} times the normal contact stiffness, k_n .

The rates of several micro-quantities (position, force, orientation, etc.) were periodically measured during the loading. These rates were calculated by first collecting the assembly's status at two instants that were separated by 100 time steps, and the difference in these states was then used to compute the rates. Because time is used in quasi-static DEM simulations as simply a means of ordering or parameterizing events, the rates of micro-quantities will

Table 3. Superscript notation

| Index | Usage |
|-------|---|
| i | A polygonal void cell having m^i edges and vertices. An m -tuple of particles or contacts, $i = (k_1, k_2, \dots, k_{m^i})$ or $i = (j_1, j_2, \dots, j_{m^i})$ |
| j | A contacting pair of particles (k_1, k_2) |
| k | A single particle |

usually be expressed in a dimensionless form by dividing by an average, macro-scale rate (average stress rate, average strain rate, etc.).

3.2

Notation

Vectors and tensors are represented by bold Roman letters, lower and upper case respectively. Their inner products are computed as

$$\mathbf{a} \cdot \mathbf{b} = a_p a_p, \quad \mathbf{A} \cdot \mathbf{B} = A_{pq} B_{pq}, \quad (1)$$

with the associated norms

$$|\mathbf{a}| = (\mathbf{a} \cdot \mathbf{a})^{1/2}, \quad |\mathbf{A}| = (\mathbf{A} \cdot \mathbf{A})^{1/2}. \quad (2)$$

A juxtaposed tensor and vector will represent the conventional product

$$\mathbf{A}\mathbf{b} = A_{pq} b_q, \quad (3)$$

and juxtaposed tensors represent the product

$$\mathbf{A}\mathbf{B} = A_{pr} B_{qr}. \quad (4)$$

Various quantities are measured at both micro and macro scales so that the variability of the micro-scale measurements can be deduced. A macro-level, assembly average is indicated with an overline ($\bar{\mathbf{L}}, \bar{\sigma}_{22}, \bar{p}_o, \bar{q}$); whereas local, micro-level quantities appear with superscripts ($\mathbf{L}^i, \boldsymbol{\sigma}^k, \hat{\mathbf{v}}^j, p^k$, Table 3). The “ k ” superscript is used with quantities that can be measured within a single particle or its immediate vicinity; the “ i ” superscript is assigned to quantities that are measured within a single void cell (the dual of particles); and the “ j ” superscript is used for quantities associated with a pair of particles or a pair of void cells (e.g. contacts, contact forces, branch vectors, and inter-particle velocities). No contractive summation is implied with superscripts, e.g. $a^j b^j$.

The non-uniformity of scalar, vector, and tensor quantities is considered in the paper. A consistent notation is used to express the conformity (or diversity) of a local quantity $\mathbf{a}^{\text{local}}$ with respect to the corresponding assembly average $\bar{\mathbf{a}}$. The pair $\mathbf{a}^{\text{local}}$ and $\bar{\mathbf{a}}$ may be scalars, vectors, or tensors. Three dimensionless scalars measure the *participation* of $\mathbf{a}^{\text{local}}$ ($= \mathbf{a}^{\text{local}} \parallel \bar{\mathbf{a}}$) in the assembly-average $\bar{\mathbf{a}}$; the *non-conformity* of $\mathbf{a}^{\text{local}}$ ($= \mathbf{a}^{\text{local}} \perp \bar{\mathbf{a}}$); and the *alignment* of $\mathbf{a}^{\text{local}}$ ($= \mathbf{a}^{\text{local}} \circ \bar{\mathbf{a}}$) with respect to the

Table 4. Statistics of uniform and random vector sets

| Measure | Vectors $\mathbf{a}^{\text{local}}$ | |
|---|-------------------------------------|---------|
| | Uniform, aligned | Random |
| $\text{Mean}(\mathbf{a}^{\text{local}} \parallel \bar{\mathbf{a}})$ | 1 | 0 |
| $\text{Std}(\mathbf{a}^{\text{local}} \parallel \bar{\mathbf{a}})$ | 0 | 1/2 |
| $\text{Mean}(\mathbf{a}^{\text{local}} \perp \bar{\mathbf{a}})$ | 0 | $2/\pi$ |
| $\text{Mean}(\mathbf{a}^{\text{local}} \circ \bar{\mathbf{a}})$ | 1 | 0 |

assembly-average $\bar{\mathbf{a}}$:

$$\mathbf{a}^{\text{local}} \parallel \bar{\mathbf{a}} = \frac{1}{|\bar{\mathbf{a}}|^2} (\mathbf{a}^{\text{local}} \cdot \bar{\mathbf{a}}) \quad (5)$$

$$\mathbf{a}^{\text{local}} \perp \bar{\mathbf{a}} = \frac{1}{|\bar{\mathbf{a}}|} |\mathbf{a}^{\text{local}} - (\mathbf{a}^{\text{local}} \parallel \bar{\mathbf{a}})\bar{\mathbf{a}}| \quad (6)$$

$$\mathbf{a}^{\text{local}} \circ \bar{\mathbf{a}} = \frac{1}{|\mathbf{a}^{\text{local}}| |\bar{\mathbf{a}}|} (\mathbf{a}^{\text{local}} \cdot \bar{\mathbf{a}}) \quad (7)$$

The participation and non-conformity in Eqs. 5 and 6 are the dimensionless magnitudes of $\mathbf{a}^{\text{local}}$ in directions parallel and perpendicular to $\bar{\mathbf{a}}$, and relative to the length of $\bar{\mathbf{a}}$. The alignment $\mathbf{a}^{\text{local}} \circ \bar{\mathbf{a}}$ is the cosine of the angle separating $\mathbf{a}^{\text{local}}$ and $\bar{\mathbf{a}}$. These quantities are unambiguous when \mathbf{a} is a vector or tensor. If \mathbf{a} is a scalar, then $\mathbf{a}^{\text{local}} \parallel \bar{\mathbf{a}}$ is simply the quotient a^{local}/\bar{a} ; $\mathbf{a}^{\text{local}} \perp \bar{\mathbf{a}}$ is zero; and $\mathbf{a}^{\text{local}} \circ \bar{\mathbf{a}}$ is $\text{sgn}(a^{\text{local}}, \bar{a})$. By reducing vector and tensor objects to the scalars in Eqs. (5–7), we can compute conventional statistical measures such as the mean, standard deviation, and coefficient of variation. These measures will be represented with the notation $\text{Mean}(\cdot)$, $\text{Std}(\cdot)$, and $\text{Cov}(\cdot)$, where the coefficient of variation $\text{Cov}(\cdot) = \text{Std}(\cdot)/\text{Mean}(\cdot)$.

As an example with vector quantities \mathbf{a} , we can consider two different sets of two-dimensional vectors $\mathbf{a}^{\text{local}}$, and this example can serve as a reference case for comparing the results given later in the paper. In both sets, the vectors $\mathbf{a}^{\text{local}}$ all have unit length. In the first set, the vectors $\mathbf{a}^{\text{local}}$ have a uniform direction that is aligned with the reference vector $\bar{\mathbf{a}}$; but in the second set, the vectors $\mathbf{a}^{\text{local}}$ have uniformly random directions. In the example, the reference vector $\bar{\mathbf{a}}$ is also assumed to have unit length. The four statistical measures $\text{Mean}(\mathbf{a}^{\text{local}} \parallel \bar{\mathbf{a}})$, $\text{Std}(\mathbf{a}^{\text{local}} \parallel \bar{\mathbf{a}})$, $\text{Mean}(\mathbf{a}^{\text{local}} \perp \bar{\mathbf{a}})$, and $\text{Mean}(\mathbf{a}^{\text{local}} \circ \bar{\mathbf{a}})$ are used in the paper as indicators of local non-conformity and heterogeneity, and their values for this simple example are summarized in Table 4. In the simulated biaxial loading of 10,816 circular disks, certain local vector and tensor quantities are found to have measured values of $\text{Std}(\mathbf{a}^{\text{local}} \parallel \bar{\mathbf{a}})$ and $\text{Mean}(\mathbf{a}^{\text{local}} \perp \bar{\mathbf{a}})$ that greatly exceed those of the random set, as given in the final column of Table 4. These large values are due to variations in the magnitudes of the local quantities as well as in their directions.

4

Heterogeneity measurements

The experimental results are analyzed for indications of four categories of heterogeneity: topologic, geometric (fabric), kinematic, and static.

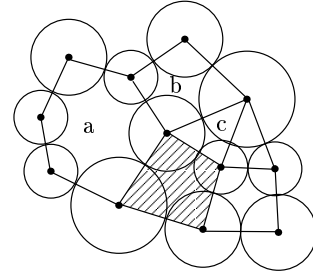


Fig. 2. Particle graph of a 2D granular assembly. A single void cell is shaded. The void cells labeled a, b, and c have valences of 6, 4, and 3 respectively.

4.1

Topologic heterogeneity

In a 2D setting, the topology of an assembly can be described by the *particle graph* of its particles (the graph vertices) and their contacts (the graph edges) [61]. The particle graph is associated with the Voronoi-Dirichlet tessellation of a 2D region, except that the particle graph admits only the real contacts as graph edges. The faces of the planar graph are polygonal void cells, which are enclosed by the circuits of contacting particles (an example void cell is shaded in Fig. 2). For this topologic description of a 2D granular material, the simplest local topologic measures are the local coordination number n^k and the local valence m^i , defined as the number of contacts of a single particle k , and the number of edges of a single void cell i (see Fig. 2 for examples of valence). Because gravity is absent in the current simulations, some particles will be unattached and, hence, excluded from the particle graph. The effective average coordination number \bar{n}_{eff} of the attached particles will be somewhat larger than the coordination number \bar{n} that includes both attached and unattached particles [9,11]. Dense assemblies have large coordination numbers and small valences, but during biaxial compression, the average effective coordination number is reduced, while the average valence increases [9,11]. In the simulation of biaxial compression, \bar{n}_{eff} is reduced from 4.14 in the initial particle arrangement to a value of 3.50 at the final compressive strain, $\bar{\epsilon}_{22} = -0.01$. The average valence \bar{m} increases from 3.87 to 4.66.

A simple measure of topologic nonuniformity is the dispersion in the local values of n^k and m^i . Figure 3 shows the evolution of the coefficients of variation of these two local topologic measures. Together, the results indicate an increase in topologic heterogeneity during loading. The large increase in the dispersion of local valence, as expressed by the coefficient of variation $\text{Cov}(m^i)$, is consistent with the results of Tsuchikura and Satake [26], who have shown that the sizes of void cells become more diverse during biaxial compression. The increase in the coefficient of variation of the local coordination number, $\text{Cov}(n^i) = \text{Std}(n^i)/\text{Mean}(n^i)$, is due, in part, to a reduction in the mean coordination number.

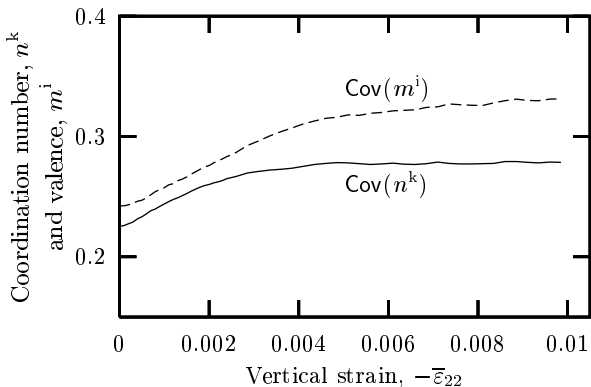


Fig. 3. The evolution of two measures of topologic heterogeneity during biaxial compression: the coefficients of variation (Cof) of the local coordination number (n^k) and local valence (m^i).

4.2 Geometric heterogeneity

Geometric characteristics of granular materials are listed in Table 1, and numerous studies have shown how the assembly averages of these characteristics evolve during loading. Fewer studies indicate how the internal diversity of these characteristics changes with loading. Tsuchikura and Satake [26] have developed methods for examining the diversity of local fabric in a 2D granular material and found that void cells become more elongated during loading, but that the variation in elongation remains fairly uniform. To study this form of fabric anisotropy, they propose a method for computing the magnitude of the anisotropy of a general second order symmetric tensor \mathbf{T} by considering its deviatoric part \mathbf{T}' . The self-product of \mathbf{T}' yields a scalar measure β of anisotropy:

$$\mathbf{T}'\mathbf{T}' = \beta^2 \mathbf{I}. \quad (8)$$

In their experimental study, they used β to measure the local anisotropy (elongation magnitude) of the loop tensors of individual void cells. The current study applies the same methods to analyze heterogeneity in the local fabric tensor.

Satake [34] proposed the fabric tensor as a measure of particle arrangement in a granular material, and we use a local form, \mathbf{F}^k , to analyze fabric heterogeneity:

$$F_{pq}^k = \frac{1}{n^k} \sum_{j=1}^{n^k} \eta_p^j \eta_q^j, \quad (9)$$

where the tensor for a particle k involves its n^k contacts. Superscript j denotes the j th contact with particle k (Table 3). Vectors $\boldsymbol{\eta}^j$ are unit vectors in the directions of the branch vectors that join the center of particle k with the centers of its contacting neighbors. The assembly average $\bar{\mathbf{F}}$ is computed from the sum of local values for all N_{eff} particles that are included in (attached to) the particle graph,

$$\bar{\mathbf{F}} = \frac{1}{2N_{\text{eff}}} \sum_{k=1}^{N_{\text{eff}}} n^k \mathbf{F}^k. \quad (10)$$

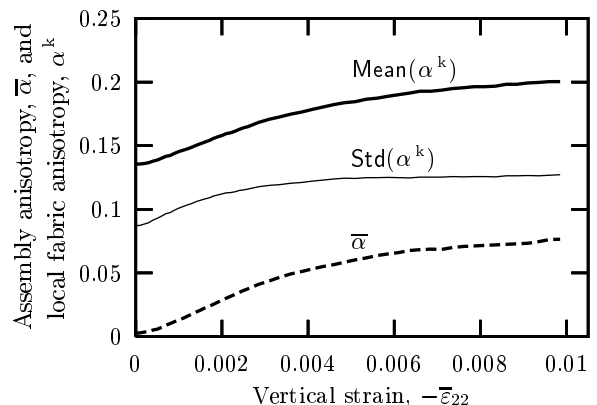


Fig. 4. Changes in the average and local fabric anisotropies during biaxial compression.

Studies have shown that $\bar{\mathbf{F}}$ becomes increasingly anisotropic during deviatoric loading, with the major principal direction of $\bar{\mathbf{F}}$ becoming more aligned with the direction of compressive loading [6, 11].

The current study considers variability in the local anisotropy of fabric. We apply Eq. 8 to the local fabric tensor \mathbf{F}^k to compute a local measure α^k of fabric anisotropy: $\mathbf{T} \rightarrow \mathbf{F}^k$, $\beta \rightarrow \alpha^k$. Fig. 4 shows the results for the biaxial compression tests. The average fabric anisotropy of the entire assembly, $\bar{\alpha}$, increases with loading (Eqs. 8 and 10), a results that is consistent with previous experiments. As would be expected, the mean local anisotropy, $\text{Mean}(\alpha^k)$, is larger than the average assembly anisotropy $\bar{\alpha}$, and the increase in local anisotropy parallels that of the entire assembly. The results also show, however, that the standard deviation of fabric anisotropy increases with strain. The increase in $\text{Std}(\alpha^k)$ suggests that the geometric arrangement of particles becomes more varied during loading.

4.3 Inter-particle movements

The change in stress within a dry granular material is due to local changes in the inter-particle forces that result from the relative shifting of particles during assembly deformation. The simplest models of this mechanism are based upon the interactions of particle pairs that are constrained to move in accord with a homogeneous deformation field. Bathurst and Rothenburg [42] studied the inter-particle movements at small strains in the biaxial compression of a disk assembly. Their results demonstrate that, on average, the inter-particle movements at small strains are less than those that would be consistent with uniform deformation (see also [39]). The current study addresses the non-conformity of inter-particle movements relative to the average deformation, the diversity of this non-conformity, its evolution during loading, and the spatial coherence of the non-conformity. In this regard, we consider only those particles that are included in the particle graph at a particular stage of loading. The relative velocity $\hat{\mathbf{v}}^j$ of two particles k_1 and k_2 is the difference in their velocities

$$\hat{\mathbf{v}}^j = \mathbf{v}^{k_2} - \mathbf{v}^{k_1}, \quad (11)$$

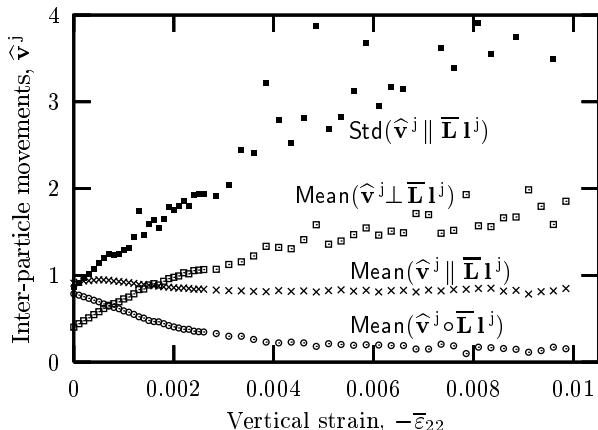


Fig. 5. Evolution of the non-conformity and heterogeneity of inter-particle motions $\hat{\mathbf{v}}^j$ during biaxial compression. The motions are for particle pairs j that are in direct contact ($\rho = 1$). Over 18,000 pairs are represented in each point.

where index j represents the contacting pair (k_1, k_2) . The relative movement that would be consistent with homogeneous deformation is the product $\bar{\mathbf{L}}\mathbf{l}^j$, where $\bar{\mathbf{L}}$ is the average velocity gradient of the assembly, and \mathbf{l}^j is the branch vector between the centers of particles k_1 and k_2 (Table 3).

The quantities in Eqs. (5–7) can be applied to describe the conformity (or non-conformity) and diversity of the local, inter-particle motions $\hat{\mathbf{v}}^j$ with respect to the mean-field displacement $\bar{\mathbf{L}}\mathbf{l}^j$. We begin by considering only pairs of particles that are in direct contact during biaxial compression (the number of these pairs ranges from 17,600 to 21,300 for the 10,816 particles), although we will consider more distant pairs in a later paragraph.

The evolution of measures (5–7) are shown in Fig. 5. The average inter-particle motions $\hat{\mathbf{v}}^j$ are consistently less than the mean-field motions, as is shown by a mean conformity $\text{Mean}(\hat{\mathbf{v}}^j \parallel \bar{\mathbf{L}}\mathbf{l}^j)$ less than 1. This result is consistent with studies [39] and [42], which investigated the local behavior at small strains. Figure 5 shows that the mean conformity, $\text{Mean}(\hat{\mathbf{v}}^j \parallel \bar{\mathbf{L}}\mathbf{l}^j)$, is modestly reduced during loading, from about 0.91 to about 0.82. As we will see, however, the diversity of the fluctuations can be quite large. Both the non-conformity and heterogeneity of inter-particle motions are indicated by the additional measures $\text{Mean}(\hat{\mathbf{v}}^j \perp \bar{\mathbf{L}}\mathbf{l}^j)$ and $\text{Mean}(\hat{\mathbf{v}}^j \circ \bar{\mathbf{L}}\mathbf{l}^j)$. If the local motions were in uniform conformance with the assembly deformation, these two measures would have values of 0 and 1 respectively. At large strains, the value of $\text{Mean}(\hat{\mathbf{v}}^j \perp \bar{\mathbf{L}}\mathbf{l}^j)$ approaches 2, compared with a value of $\text{Mean}(\hat{\mathbf{v}}^j \parallel \bar{\mathbf{L}}\mathbf{l}^j)$ of about 0.82. These results reveal that, on average and at large strains, the components of inter-particle movements that are *orthogonal* to their mean-field directions can be more than twice as large as the components that are aligned with the mean-field directions (Eqs. 5 and 6). This lack of vector alignment is also indicated by the cosine-type measure $\text{Mean}(\hat{\mathbf{v}}^j \circ \bar{\mathbf{L}}\mathbf{l}^j)$, which is reduced to a value of about 0.15 (see Eq. 7). At the end of the test, fully 40% of inter-particle motions were in the “wrong” direction, with values $\hat{\mathbf{v}}^j \cdot (\bar{\mathbf{L}}\mathbf{l}^j) < 0$. The fourth measure in Fig. 5 is $\text{Std}(\hat{\mathbf{v}}^j \parallel \bar{\mathbf{L}}\mathbf{l}^j)$, which displays a rather extreme degree of

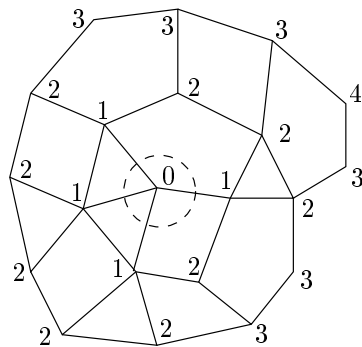


Fig. 6. Discrete distances ρ from a reference particle 0. The vertices represent particle centers; edges represent particle contacts.

nonuniformity in the components of inter-particle movements that are parallel to the mean-field directions. This nonuniformity is particularly sizable at large strains. A set of random vectors of uniform length would have a value of $\text{Std}(\hat{\mathbf{v}}^j \parallel \bar{\mathbf{L}}\mathbf{l}^j)$ of only 0.5 (Table 4), a value several times smaller than those in Fig. 5. Such large values indicate a substantial heterogeneity in both the magnitudes and directions of the inter-particle movements $\hat{\mathbf{v}}^j$.

We can also use the biaxial compression simulation to investigate the spatial correlation of inter-particle movements and the length scale at which the inter-particle movements approximate the mean deformation field. Kruyt and Rothenburg [39] measured the spatial correlation of movements at small strains by using a 2-point correlation technique. In the current study, we do not consider all possible particle pairs, but instead use only those pairs of particles that are included in (attached to) the particle graph, as only these particles participate directly in the deformation and load-bearing mechanisms. This limitation suggests a *discrete metric* ρ for describing the distance between two particles k_1 and k_2 . The distance $\rho(k_1, k_2)$ is the least number of contacts (graph edges) that must be traversed to connect k_1 and k_2 (Fig. 6). The results in Fig. 5, which have already been described, were collected from the sets of all particle pairs at a discrete distance of 1, i.e. the sets $\{(k_1, k_2) : \rho(k_1, k_2) = 1\}$ at various stages of loading. The discrete metric does not provide angle or size, so all subsequent calculations with the objects $\hat{\mathbf{v}}^j$, $\bar{\mathbf{L}}$, and \mathbf{l}^j were, of course, performed in Euclidean space, but only on the selected particle pairs.

Figure 7 shows the non-conformity and heterogeneity of inter-particle movements $\hat{\mathbf{v}}^j$ for particle pairs j at distances ρ of 1 to 10, but at the single large strain $\bar{\epsilon}_{22} = -0.005$ (see Fig. 1). (The results for $\rho = 10$ involve over one-quarter million particle pairs.) As would be expected, the average conformity of the observed inter-particle movements with their corresponding mean-strain movements improves with an increasing discrete distance between the pairs. This improved conformity is evidenced by increases in the measures $\text{Mean}(\hat{\mathbf{v}}^j \parallel \bar{\mathbf{L}}\mathbf{l}^j)$ and $\text{Mean}(\hat{\mathbf{v}}^j \circ \bar{\mathbf{L}}\mathbf{l}^j)$ and in the reduction of $\text{Mean}(\hat{\mathbf{v}}^j \perp \bar{\mathbf{L}}\mathbf{l}^j)$. However, at a distance of $\rho = 10$ and at the strain $\bar{\epsilon}_{22} = -0.005$, the values of these three measures are about the same as those at distance $\rho = 1$ with zero strain, $\bar{\epsilon}_{22} \approx 0$. That is, at the large strain of -0.005 , the non-conformity of motion at a dis-

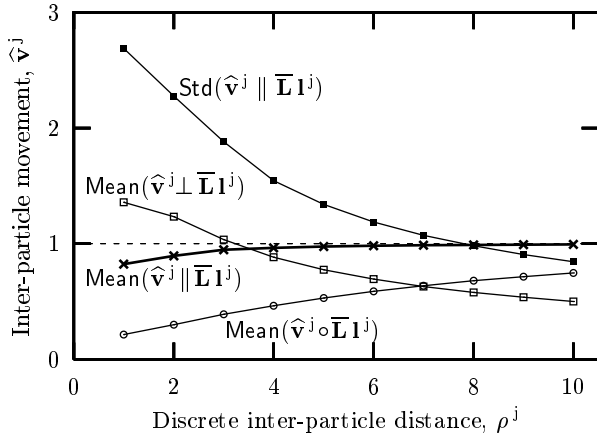


Fig. 7. The correlation of inter-particle motions with the discrete distance ρ between particle pairs at a strain $\bar{\varepsilon}_{22} = -0.005$. The superscript j represents a pair of particles (k_1, k_2) that are separated by distance ρ . The results at $\rho = 1$ involve 18,000 pairs; results at $\rho = 10$ involve over 250,000 pairs.

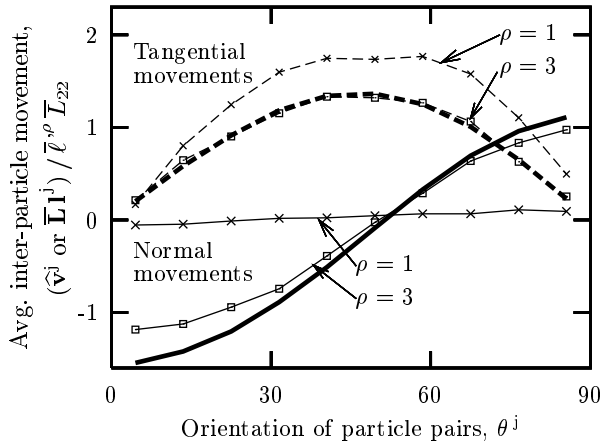


Fig. 8. The average normal and tangential motions of particle pairs as a function of the pair orientation θ^j . Mean-field motions $\bar{\mathbf{L}}^j$ are represented by heavy lines; whereas, the averaged actual inter-particle motions are the lighter lines. Values are given for pairs having discrete distances ρ of 1 and 3. The compressive strain $\bar{\varepsilon}_{22}$ is -0.005 (see Fig. 1).

tance of about 8–10 particle diameters is no better than the modestly substantial non-conformity of neighboring particles at small strains.

The conformity between the actual and mean-field motions is particularly poor at large strains if we consider only the *normal* motions between the particle pairs that are in direct contact (i.e. with $\rho = 1$). Figure 8 shows the assembly averages of the normal and tangential motions of those particle pairs that are separated by distances ρ of 1 and 3, at the large strain $\bar{\varepsilon}_{22} = -0.005$. These motions are plotted against the orientation angles θ^j of the pairs (Fig. 9), and advantage has been taken of the loading symmetry by folding the angles θ^j into the single quadrant 0° to 90° . The normal inter-particle motions are the inner products $\hat{\mathbf{v}}^j \cdot \boldsymbol{\eta}^j$, where $\boldsymbol{\eta}^j$ is the unit vector aligned with the branch vector \mathbf{l}^j that connects the centers of a particle pair $j = (k_1, k_2)$. Figure 8 compares the averages of these values with the corresponding averages of the mean-

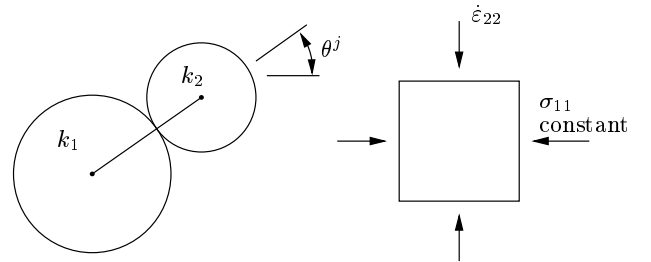


Fig. 9. Orientation angle θ^j for a particle pair.

field motions $\bar{\mathbf{L}}^j$ (the latter are represented with heavy lines). The results have been normalized by dividing by the average length $\ell^{\rho} = \langle |\mathbf{l}^{j,\rho}| \rangle$ for a particular separation ρ and by the strain rate \bar{L}_{22} . Figure 8 shows that, at large strains, the movements of contacting particles ($\rho = 1$) are predominantly tangential, and that the mean normal motion is quite small. That is, at $\rho = 1$ and at large strains, the normal inter-particle movements are grossly overestimated by the mean-field motion $\bar{\mathbf{L}}^j$. At a distance $\rho = 3$, the motions are, on average, in much closer conformity with those predicted by a mean-field assumption. The apparent conformity at $\rho = 3$ in Fig. 8 is, however, based upon an average of movements, and the true diversity in their values is more appropriately reflected in the measures $\text{Mean}(\hat{\mathbf{v}}^j \perp \bar{\mathbf{L}}^j)$, $\text{Mean}(\hat{\mathbf{v}}^j \circ \bar{\mathbf{L}}^j)$, and $\text{Std}(\hat{\mathbf{v}}^j \parallel \bar{\mathbf{L}}^j)$, which are reported in Figs. 5 and 7.

4.4 Deformation heterogeneity

Micro-scale deformations within a 2D granular material can be computed by considering the small polygonal void cells as being representative micro-regions among particle clusters (Fig. 2) [62,63,9]. The region of 10,816 particles can be partitioned into over 7500 of these void cells. The average velocity gradient \mathbf{L}^i within a single polygonal void cell i is computed from the motions of the particles at its vertices. These local velocity gradients can then be compared with the average assembly gradient $\bar{\mathbf{L}}$, and the measures in Eqs. (5–7) can be used to investigate the non-conformity and heterogeneity of local deformations. Figure 10 shows the evolution of these measures in the course of a biaxial compression test. At small strains, the local deformations are modestly aligned with the averaged deformation: the average cosine of alignment, $\text{Mean}(\mathbf{L}^i \circ \bar{\mathbf{L}})$, is 0.91, only slightly lower than 1, and the average component of the local gradient \mathbf{L}^i that is perpendicular to the assembly average $\bar{\mathbf{L}}$ is about 35% of $|\bar{\mathbf{L}}|$. At larger strains, the local deformations are, on average, far more deviant and exhibit a much larger dispersion of values. The standard deviation of the aligned deformations, $\text{Mean}(\mathbf{L}^i \parallel \bar{\mathbf{L}})$, becomes more than twice its mean value of 1. Deformations that are orthogonal to $\bar{\mathbf{L}}$ become, on average, much larger than those parallel to $\bar{\mathbf{L}}$ (compare the $\text{Mean}(\mathbf{L}^i \perp \bar{\mathbf{L}})$ in Fig. 10 with a $\text{Mean}(\mathbf{L}^i \parallel \bar{\mathbf{L}})$ of 1).

This non-conformity and heterogeneity is also illustrated in Fig. 11, which shows the distributions of aligned deformations at moderate and large compressive strains, $\bar{\varepsilon}_{22}$ of -0.0005 and -0.005 . In each figure, the void cells

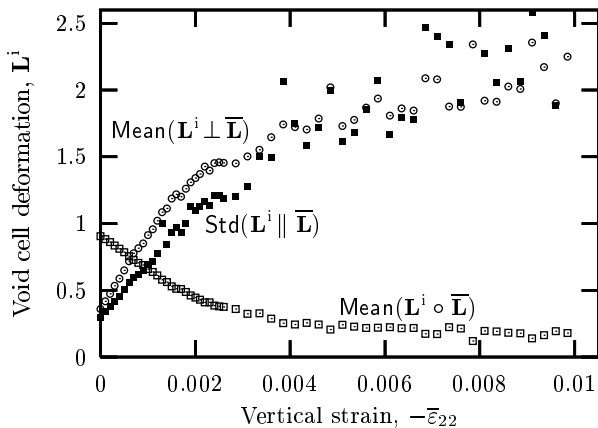
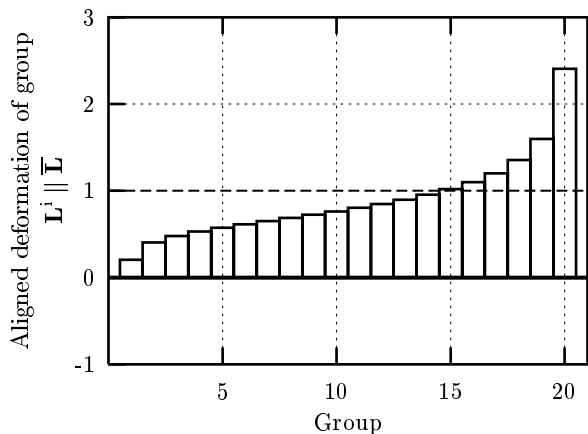
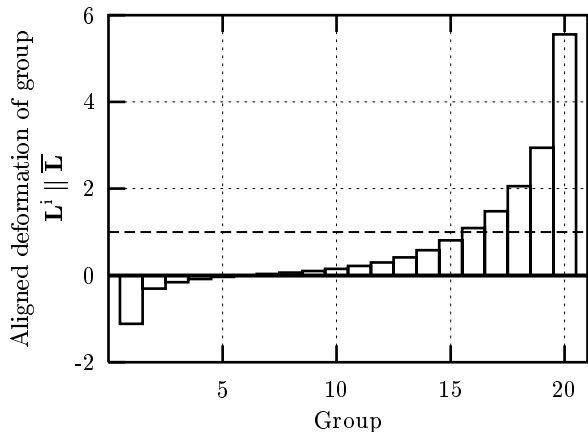


Fig. 10. The evolution of deformation non-conformity and heterogeneity during biaxial compression. Each point represents the deformations \mathbf{L}^i in over 7500 void cells, where superscript i represents an i th void cell.



(a) $\bar{\epsilon}_{22} = -0.0005$



(b) $\bar{\epsilon}_{22} = -0.005$

Fig. 11. Distributions of the aligned deformation of void cells at two strains. The void cells have been grouped according to a ranking of their $\mathbf{L}^i \parallel \bar{\mathbf{L}}$ values (10,900 and 8300 void cells are included at the two strains).

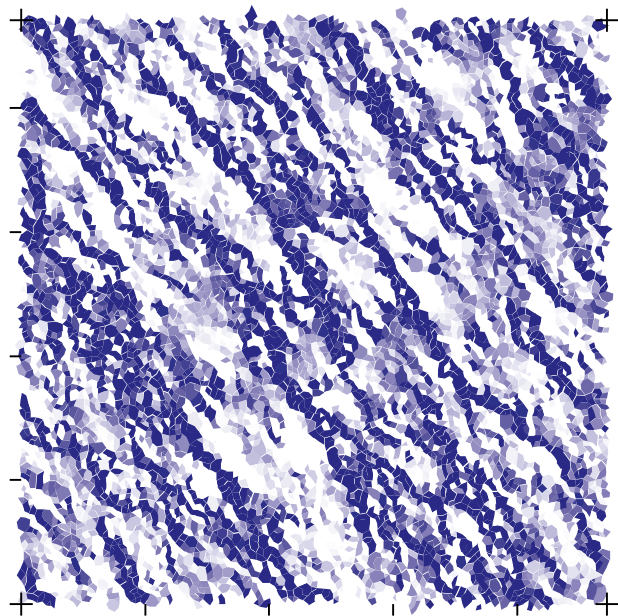


Fig. 12. The presence of right-shear microbands at strain $\bar{\epsilon}_{22} = -0.0005$. The local void cell deformations \mathbf{L}^i have been filtered as $\mathbf{L}^i \Phi$, where the filter $\Phi = [0.49 \ 0.41; -0.58 \ -0.49]$ captures a deformation mode that produces shearing that is downward and to the right. A complementary set of left-shear microbands would be present with the use of an alternative filter. The gray scale illustrates the magnitudes of the local filtered deformations, but some of the white regions have negative filtered values in this monochrome plot.

have been placed into 20 bins, arranged according to a ranking of the aligned deformations $\mathbf{L}^i \parallel \bar{\mathbf{L}}$ of each, i th void cell. At moderate strains, the 10% of most contributory void cells participate disproportionately in the average assembly deformation and about 6.5 times more than the lowest 10% of void cells (Fig. 11a). At the larger strain of -0.005 , about 22% of the material makes a *negative* contribution to the overall assembly deformation, and, in a sense, is deforming in the “wrong” direction (Fig. 11b). As another measure of this heterogeneity at large strain, the 31% of most contributory void cells could account, by themselves, for the entire assembly deformation. This situation is akin to that of a material in which a shear band has developed, where intense shearing within the band is accompanied by unloading outside of the band. No shear bands were observed in the current simulations, although another type of localization, in the form of multiple non-persistent *micro-bands*, was present throughout the biaxial compression test. This type of deformation patterning, described in [9], was subtly present at the start of deformation and became more pronounced as deformation proceeded. Microband localization accounts for much of the deformation heterogeneity that is recorded in Figs. 10 and 11. An example of micro-band patterning at small strain is shown in Fig. 12, in which the local, void cell deformations \mathbf{L}^i have been filtered to highlight a right-shear deformation mode (see [9] for a discussion of the visualization technique).

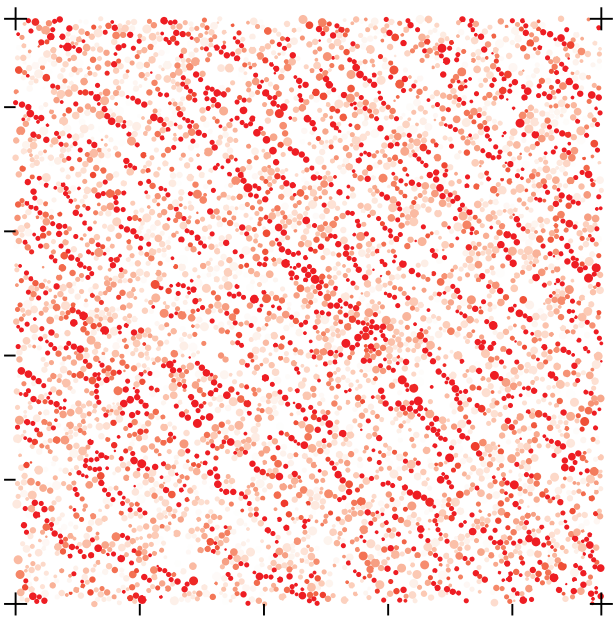


Fig. 13. Particle spins in a biaxial compression test at strain $\bar{\epsilon}_{22} = -0.0005$. Only clockwise spinning particles are shown in the plot.

4.5

Particle rotation heterogeneity

Particle rotations in granular materials are known to be large, particularly in 2D assemblies of circular disks. De-decker et al. [44] found that the standard deviation of the particle rotation rates could be several times larger than the average strain rate of an assembly. Calvetti et al. [30] reported that the variability of particle rotations increased consistently with increasing strain. Figure 13 shows that this variability is expressed in a spatial patterning of particle rotations. The figure is taken at the moderate strain $\bar{\epsilon}_{22}$ of -0.0005 , but *only counter-clockwise* rotations are shown in this monochrome plot, where the shading depends upon the dimensionless rotation rate $\omega^k/|\bar{\mathbf{L}}|$. The most rapidly rotating particles are usually aligned in chain-like patterns oblique to the principal stress directions. These chains are closely associated with microbands, as can be seen by comparing Figs. 12 and 13 [9].

4.6

Stress heterogeneity

The transmission of force among particles occurs in a non-uniform manner, with certain chains of particles bearing a disproportionate share of the surface tractions. These force chains have been widely observed, and several related references are given in Table 1. The current study concerns the distribution of *stress* among an assembly's particles. In two previous studies, the local variation of stress within stacks of rods has been studied by withdrawing groups of rods and measuring the removal force [58, 57]. The DEM simulations of the current study allow the

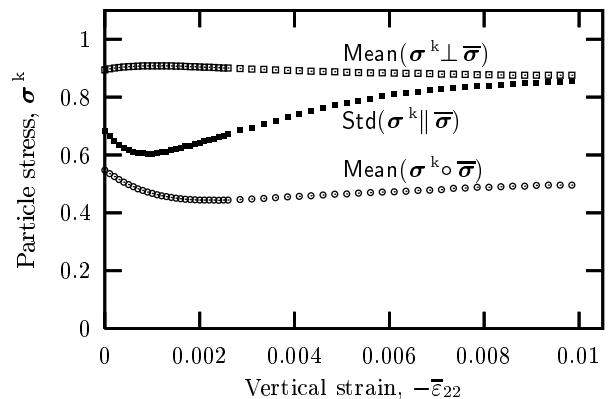


Fig. 14. The evolution of stress non-conformity and heterogeneity during biaxial compression.

direct computation of stress σ^k within each, k th disk:

$$\sigma_{pq}^k = \frac{r^k}{A^k} \sum_{j=1}^{n^k} \eta_p^j f_q^j, \quad (12)$$

where summation is over the n^k contacts j of the particle k , r^k is the disk radius, η^k is the unit normal vector, and \mathbf{f}^j is the contact force. Satake [64] and Kruyt and Rothenburg [39] have described a dual of the particle graph that could be used to compute a representative particle area A^k that includes a portion of the void space around a particle. To compute a local stress that can be compared with the average assembly stress, we instead use the (solid) disk area $\pi(r^k)^2$ and simply divide it by the assembly-average solid fraction.

Figure 14 shows the evolution of non-conformity and heterogeneity in the local stress σ^k (eqs. 5–7). The average, cosine-type alignment of the local stress, $\text{Mean}(\sigma^k \circ \bar{\sigma})$, is less than 0.6, but there is little change in this average alignment during loading. The spatial variation in local stress, as measured by $\text{Std}(\sigma^k \parallel \bar{\sigma})$, decreases at small strains, but then increases at larger strains. At large strains, all three measures in Fig. 14 depict a greater conformity and homogeneity of stress than was found with inter-particle movements and void cell deformations (*cf* Figs. 5, 10 and 14). This greater regularity is likely due to the stress being represented in its status, whereas movement and deformation were represented in their rates. At small strains, however, the three measures in Fig. 14 show less conformity and heterogeneity in stress than in the inter-particle movements. The diversity of stress at small strain is primarily the inheritance of the initial particle packing, and this diversity increases only modestly during loading.

The variation in stress is greatest in its deviatoric component. Figures 15a and 15b are histograms of the local mean stress and deviator stress, defined for particle k as $p^k = (\sigma_{11}^k + \sigma_{22}^k)/2$ and $q^k = (\sigma_{22}^k - \sigma_{11}^k)/2$ respectively. The figure gives these components at the large strain $\bar{\epsilon}_{22} = -0.005$. Because only compressive force can be delivered between particles, the local mean stress is uniformly positive, but the standard deviation of the local mean stress p^k is about 0.60 (Fig. 15a). The standard deviation of the local deviator stress q^k is 1.0 (Fig. 15b).

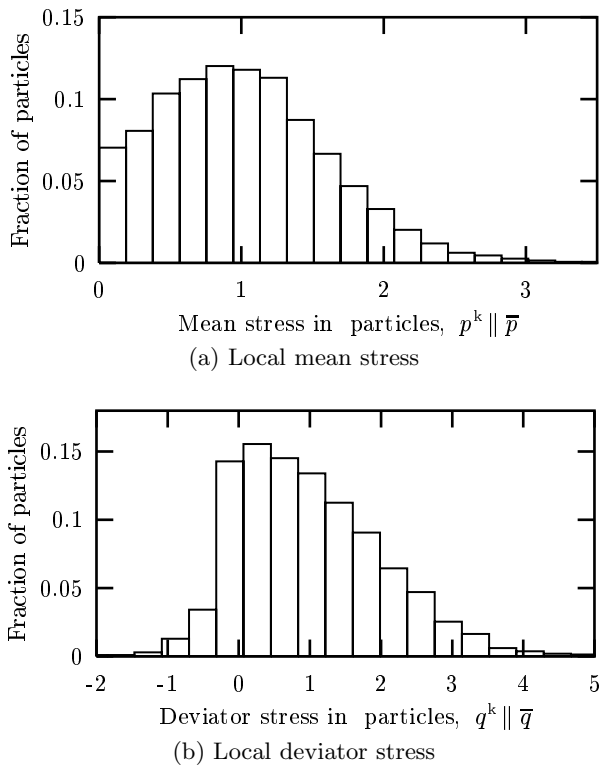


Fig. 15. Participation of the local stress in the average assembly stress. Figures 15a and 15b are histograms of the local participation in the mean and deviator stresses. Both figures are compiled from the stresses in over 10,000 particles at the large strain $\bar{\epsilon}_{22} = -0.005$.

About 15% of particles have a negative alignment of the deviator stress, $q^k \parallel \bar{q}$, and these particles provide a negative contribution toward bearing the average assembly deviator stress.

5

Conclusion

In the paper, we have considered several categories of heterogeneity in granular materials: topologic, geometric, kinematic, and static. In all respects, the heterogeneity can be described, at a minimum, as being moderate. Heterogeneity increases during biaxial compressive loading. In the case of inter-particle movements, the non-uniformity becomes extreme, and particle motions are only coarsely aligned with the mean-field movement. At large strains, significant fluctuations from the mean-field motion extend to distances of at least eight particle diameters. Non-uniform motion is expressed in the patterning of local movements, which includes microband patterning and rotation chain patterning. The extent and magnitude of the heterogeneity and its patterning proffer an imposing challenge to the continuum representation of granular materials at micro and macro scales, especially at large strains. Before such efforts can be productive, further statistical analyses should be undertaken to further characterize heterogeneity, to determine characteristic lengths at which heterogeneity dominates the meso-scale behavior, to quantify the heterogeneity in the local stress rates, and

to establish the relationships among topologic, geometric, kinematic, and static heterogeneities.

References

1. W. O. Smith, P. D. Foote, and P. F. Busang. Packing of homogeneous spheres. *Physical Review*, 34(9):1271–1274, 1929.
2. M. Oda. Co-ordination number and its relation to shear strength of granular material. *Soils and Found.*, 17(2):29–42, June 1977.
3. J. Lemaitre, A. Gervois, J. P. Troadec, N. Rivier, M. Ammi, L. Oger, and D. Bideau. Arrangement of cells in Voronoi tessellations of monosize packing of discs. *Phil. Mag. B*, 67(3):347–362, 1993.
4. R. Y. Yang, R. P. Zou, and A. B. Yu. Computer simulation of the packing of fine particles. *Physical Rev. E*, 62(3):3900–3908, 2000.
5. P. Chapius. *De la structure géométrique des milieux granulaires en relation avec leur comportement mécanique*. Thesis, Ecole Polytechnique, Montreal, Canada, 1976.
6. M. Oda, J. Konishi, and S. Nemat-Nasser. Experimental micromechanical evaluation of strength of granular materials: Effects of particle rolling. *Mech. of Materials*, 1(4):269–283, 1982.
7. R. J. Bathurst and L. Rothenburg. Observations on stress-force-fabric relationships in idealized granular materials. *Mech. of Materials*, 9:65–80, 1990.
8. Y.-C. Chen. Effect of inter-particle friction and initial fabric on fabric evolution. *J. Chinese Inst. Engrs.*, 13(2):147–156, 1990.
9. M. R. Kuhn. Structured deformation in granular materials. *Mech. of Materials*, 31(6):407–429, 1999.
10. B. Cambou, M. Chaze, and F. Dedecker. Change of scale in granular materials. *Eur. J. Mech. A/Solids*, 19(6):999–1014, 2000.
11. C. Thornton. Numerical simulations of deviatoric shear deformation of granular media. *Géotechnique*, 50(1):43–53, 2000.
12. C. Annic, D. Bideau, J. Lemaitre, J. P. Troadec, and A. Gervois. Geometrical properties of 2D packings of particles. In C. Thornton, editor, *Powders & Grains 93*, pages 11–16. A.A. Balkema, Rotterdam, The Netherlands, 1993.
13. M. Oda. Deformation mechanism of sand in triaxial compression tests. *Soils and Found.*, 12(4):45–63, 1972.
14. M. Oda. Geometrical properties of 2D packings of particles. In C. Thornton, editor, *Powders & Grains 93*, pages 161–166. A.A. Balkema, Rotterdam, The Netherlands, 1993.
15. T.-T. Ng. Fabric evolution of ellipsoidal arrays with different particle shapes. *J. Engrg. Mech.*, 127(10):994–999, 2001.
16. M. Oda. Initial fabrics and their relations to mechanical properties of granular material. *Soils and Found.*, 12(1):17–36, Mar. 1972.
17. L. Rothenburg and R.J. Bathurst. Micromechanical features of granular assemblies with planar elliptical particles. *Géotechnique*, 42(1):79–95, 1992.
18. T. Matsushima and K. Konagai. Grain-shape effect on peak strength of granular materials. In C. S. Desai, T. Kundu, S. Harpalani, and J. Kennedy, editors, *Computer Methods and Advances in Geomechanics, Proceedings of the 10th International Conference on Computer Methods and Advances in Geomechanics*, pages 361–366. A. A. Balkema, Rotterdam, 2001.

19. T. Mogami. A statistical approach to the mechanics of granular materials. *Soils and Found.*, 6(1):26–36, Jan. 1966.
20. E. L. Hinrichsen, Feder J., and T. Jossang. Random packing of disks in two dimensions. *Phy. Rev. A*, 41(8):4199–4209, 1990.
21. J. P. Bardet and J. Proubet. A numerical investigation of the structure of persistent shear bands in granular media. *Géotechnique*, 41(4):599–613, 1991.
22. J. Desrues, R. Chambon, M. Mokni, and F. Mazeur. Void ratio evolution inside shear bands in triaxial sand specimens studied by computed tomography. *Géotechnique*, 46(3):529–546, 1996.
23. K. Iwashita and M. Oda. Rolling resistance at contacts in simulation of shear band development by DEM. *J. Engrg. Mech.*, 124(3):285–292, Mar. 1998.
24. S. Sture, N. C. Costes, S. N. Batiste, M. R. Lankton, K. A. Alshibli, B. Jeremic, R. A. Swanson, and M. Frank. Mechanics of granular materials at low effective stresses. *J. Aerospace Engrg.*, 11(3):67–72, 1998.
25. J. D. Frost and D.-J. Jang. Evolution of sand microstructure during shear. *J. Engrg. Mech.*, 126(2):116–130, 2000.
26. T. Tsuchikura and M. Satake. A consideration on the statistical analysis of particle packing using loop tensors. In Y. Kishino, editor, *Powders and Grains 2001*, pages 29–32. A.A. Balkema, Lisse, 2001.
27. L. Rothenburg and R.J. Bathurst. Influence of particle eccentricity on micromechanical behavior of granular materials. *Mech. of Materials*, 16:141–152, 1993.
28. L. B. Wang, J. D. Frost, and J. S. Lai. Quantification of doublet vector distribution of granular materials. *J. Engrg. Mech.*, 127(7):720–729, 2001.
29. L. Rothenburg and R.J. Bathurst. Effects of particle shape on micromechanical behavior of granular materials. In H.H. Shen, M. Satake, M. Mehrabadi, C.S. Chang, and C.S. Campbell, editors, *Advances in micromechanics of granular materials*, pages 343–352. Elsevier, Amsterdam, The Netherlands, 1992.
30. F. Calvetti, G. Combe, and J. Lanier. Experimental micromechanical analysis of a 2D granular material: relation between structure evolution and loading path. *Mech. of Cohesive-Frictional Mat.*, 2(2):121–163, 1997.
31. D. Daudon, J. Lanier, and M. Jean. A micro mechanical comparison between experimental results and numerical simulation of a biaxial test on 2D material. In R. P. Behringer and J. T. Jenkins, editors, *Powders & Grains 97*, pages 219–222. A. A. Balkema, Rotterdam, Netherlands, 1997.
32. N. P. Kruyt and L. Rothenburg. Micromechanics of the elastic behaviour of granular materials. In P. A. Vermeer, S. Diebels, W. Ehlers, H. J. Herrmann, S. Luding, and E. Ramm, editors, *Continuous and Discontinuous Modelling of Cohesive-Frictional Materials*, pages 129–142. Springer, Berlin, 2001.
33. M. Oda, J. Konishi, and S. Nemat-Nasser. Some experimentally based fundamental results on the mechanical behaviour of granular materials. *Géotechnique*, 30(4):479–495, 1980.
34. M. Satake. Fabric tensor in granular materials. In P. A. Vermeer and H. J. Luger, editors, *Proc. IUTAM Symp. on Deformation and Failure of Granular Materials*, pages 63–68. A.A. Balkema, Rotterdam, 1982.
35. J. Konishi and F. Naruse. A note on fabric in terms of voids. In M. Satake and J.T. Jenkins, editors, *Micromechanics of Granular Materials*, pages 39–46. Elsevier Science Pub. B.V., Amsterdam, The Netherlands, 1988.
36. S. Masson and J. Martinez. Micromechanical analysis of the shear behavior of a granular materials. *J. Engrg. Mech.*, 127(10):1007–1016, 2001.
37. K. Bagi. On the definition of stress and strain in granular assemblies through the relation between micro- and macro-level characteristics. In C. Thornton, editor, *Powders & Grains 93*, pages 117–121. A.A. Balkema, Rotterdam, 1993.
38. B. Cambou and Ph. Dubujet. Difficulties and limitation of statistical homogenization in granular materials. In P. A. Vermeer, S. Diebels, W. Ehlers, H. J. Herrmann, S. Luding, and E. Ramm, editors, *Continuous and Discontinuous Modelling of Cohesive-Frictional Materials*, pages 205–214. Springer, Berlin, 2001.
39. N. P. Kruyt and L. Rothenburg. Micromechanical bounds for the effective elastic moduli of granular materials. *Int. J. Solids and Structures*, 39:311–324, 2002.
40. J. R. Williams and N. Rege. The development of circulation cell structures in granular materials undergoing compression. *Powder Technology*, 90(3):187–194, Mar. 1997.
41. A. Misra and H. Jiang. Measured kinematic fields in the biaxial shear of granular materials. *Computers and Geotechnics*, 20(3):267–285, 1997.
42. R. J. Bathurst and L. Rothenburg. Micromechanical aspects of isotropic granular assemblies with linear contact interactions. *J. Appl. Mech.*, 55(1):17–23, 1988.
43. J. P. Bardet. Observations on the effects of particle rotations on the failure of idealized granular materials. *Mech. of Materials*, 18(2):159–182, 1994.
44. F. Dedecker, M. Chaze, Ph. Dubujet, and B. Cambou. Specific features of strain in granular materials. *Mech. of Cohesive-Frictional Mat.*, 5(3):173–179, 2000.
45. H. Matsuoka. A microscopic study on shear mechanism in granular materials. *Soils and Found.*, 14(1):29–43, Mar. 1974.
46. C. Thornton. Induced anisotropy and energy dissipation in particulate material—results from computer-simulated experiments. In J. P. Boehler, editor, *Yielding, Damage, and Failure of Anisotropic Solids*, pages 113–130. Mechanical Engineering Pub., London, 1990.
47. S. J. Antony. Evolution of force distribution in three-dimensional granular media. *Phy. Rev. E*, 63(1):011302–1–13, 2000.
48. P. A. Cundall, J. T. Jenkins, and I. Ishibashi. Evolution of elastic moduli in a deforming granular assembly. In J. Biarez and R. Gourvès, editors, *Powders & Grains*, pages 319–322. A. A. Balkema, Rotterdam, The Netherlands, 1989.
49. M. Gherbi, R. Gourvès, and F. Oudjehane. Distribution of the contact forces inside a granular material. In C. Thornton, editor, *Powders & Grains 93*, pages 167–171. A.A. Balkema, Rotterdam, The Netherlands, 1993.
50. F. Radjai, D. E. Wolf, S. Roux, M. Jean, and J. J. Moreau. Force networks in dense granular media. In R. P. Behringer and J. T. Jenkins, editors, *Powders & Grains 97*, pages 211–214. A. A. Balkema, Rotterdam, Netherlands, 1997.
51. F. Radjai, D.E. Wolf, M. Jean, and J.-J. Moreau. Bimodal character of stress transmission in granular packings. *Physical Rev. Letters*, 80(1):61–64, Jan. 1998.
52. D. M. Mueth, H. M. Jaeger, and S. R. Nagel. Force distribution in a granular medium. *Physical Rev. E*, 57(3):3164–3168, 1998.
53. L. Oger, S. B. Savage, D. Corriveau, and M. Sayed. Yield and deformation of an assembly of disks subjected to a deviatoric stress loading. *Mech. of Materials*, 27(4):189–210, 1998.

54. F. Calvetti and F. Emeriault. Interparticle forces distribution in granular materials: Link with the macroscopic behaviour. *Mech. of Cohesive-Frictional Mat.*, 4(3):247–279, 1999.
55. N. P. Kruyt and L. Rothenburg. Probability density functions of contact forces for cohesionless frictional granular materials. *Int. J. Solids and Structures*, 39:571–583, 2002.
56. G. de Josselin de Jong and A. Verruijt. Étude photoélastique d’un empilement de disques. *Cahiers du Groupe Français de Rhéologie*, 7(3):73–86, 1969.
57. G. Auvinet. Stress transfer within granular geomaterials. In *Proc. of Engineering Mechanics*, pages 159–162, New York, 1992. ASCE.
58. C. Bacconnet and R. Gourves. Random aspect of the stress inside granular media. In *Proc. of Engineering Mechanics*, pages 163–166, New York, 1992. ASCE.
59. N. Gaspar and M. A. Koenders. Estimates of the shear modulus of a granular assembly using heterogeneous media techniques. In Y. Kishino, editor, *Powders and Grains 2001*, pages 389–392. A.A. Balkema, Lisse, 2001.
60. N. Gaspar. *Structures and Heterogeneity in Deforming, Densely Packed Granular Materials*. Ph.D. thesis, Kingston University, Kingston, U.K., 2002.
61. M. Satake. New formulation of graph-theoretical approach in the mechanics of granular materials. *Mech. of Materials*, 16:65–72, 1993.
62. K. Bagi. Stress and strain in granular assemblies. *Mech. of Materials*, 22(3):165–177, 1996.
63. N. P. Kruyt and L. Rothenburg. Micromechanical definition of the strain tensor for granular materials. *J. Appl. Mech.*, 118(3):706–711, 1996.
64. M. Satake. A discrete-mechanical approach to granular materials. *Int. J. Engng. Sci.*, 30(10):1525–1533, 1992.